The effects of methanol clustering on methanol–water nucleation Θ

Special Collection: Nucleation: Current Understanding Approaching 150 Years After Gibbs

Tong Sun; Gerald Wilemski 🗓 ; Barbara N. Hale; Barbara E. Wyslouzil 🗷 👵



J. Chem. Phys. 157, 184301 (2022) https://doi.org/10.1063/5.0120876





CrossMark

Articles You May Be Interested In

Improving the reproduction of an operatic performance in an IMAX cinema

J Acoust Soc Am (May 2017)

Molecular dynamics simulations of nano-confined methanol and methanol-water mixtures between infinite graphite plates: Structure and dynamics

J. Chem. Phys. (April 2019)

Methanol nucleation in a supersonic nozzle

J. Chem. Phys. (August 2011)







The effects of methanol clustering on methanol-water nucleation

Cite as: J. Chem. Phys. 157, 184301 (2022); doi: 10.1063/5.0120876 Submitted: 15 August 2022 • Accepted: 17 October 2022 •







Published Online: 8 November 2022

Tong Sun,¹ Gerald Wilemski,² D Barbara N. Hale,² and Barbara E. Wyslouzil^{1,3,a)} D



AFFILIATIONS

- ¹ William G. Lowrie Department of Chemical and Biomolecular Engineering, The Ohio State University, Columbus, Ohio 43210, USA
- ²Department of Physics, Missouri University of Science and Technology, Rolla, Missouri 65409, USA
- Department of Chemistry and Biochemistry, The Ohio State University, Columbus, Ohio 43210, USA

Note: This paper is part of the JCP Special Topic on Nucleation: Current Understanding Approaching 150 Years After Gibbs.

a) Author to whom correspondence should be addressed: Wyslouzil.1@osu.edu

ABSTRACT

The formation of subcritical methanol clusters in the vapor phase is known to complicate the analysis of nucleation measurements. Here, we investigate how this process affects the onset of binary nucleation as dilute water-methanol mixtures in nitrogen carrier gas expand in a supersonic nozzle. These are the first reported data for water-methanol nucleation in an expansion device. We start by extending an older monomer-dimer-tetramer equilibrium model to include larger clusters, relying on Helmholtz free energy differences derived from Monte Carlo simulations. The model is validated against the pressure/temperature measurements of Laksmono et al. [Phys. Chem. Phys. 13, 5855 (2011)] for dilute methanol-nitrogen mixtures expanding in a supersonic flow prior to the appearance of liquid droplets. These data are well fit when the maximum cluster size i_{max} is 6-12. The extended equilibrium model is then used to analyze the current data. On the addition of small amounts of water, heat release prior to particle formation is essentially unchanged from that for pure methanol, but liquid formation proceeds at much higher temperatures. Once water comprises more than ~24 mol % of the condensable vapor, droplet formation begins at temperatures too high for heat release from subcritical cluster formation to perturb the flow. Comparing the experimental results to binary nucleation theory is challenged by the need to extrapolate data to the subcooled region and by the inapplicability of explicit cluster models that require a minimum of 12 molecules in the critical

Published under an exclusive license by AIP Publishing. https://doi.org/10.1063/5.0120876

I. INTRODUCTION

Methanol is known to form clusters (i-mers) in both the vapor and liquid phases.¹⁻⁶ As the lowest molecular weight organic compound that can form specific structures via hydrogen bonding, the properties of methanol clusters have attracted extensive research attention in both theoretical^{7–9} and experimental studies. ^{10–13}

In the vapor phase, the presence of clusters—or vapor phase polymers—leads to an anomalous dependence of the heat capacity on pressure. When analyzing their temperature and pressure dependent calorimetric measurements, Weltner and Pitzer¹⁴ assumed the vapor consisted of monomer/dimer/tetramer mixtures in local equilibrium and estimated both the enthalpy and entropy of dimer and tetramer formation. Under Weltner and Pitzer's experimental conditions, however, the model could not distinguish between mixtures

comprised of monomer/dimer/tetramer only, and mixtures comprised of monomer, dimer and a mixture of higher i-mers. In complementary experiments, Renner et al. 15 measured thermal conductivity data as a function of temperature and pressure. Fits to models that treated the vapor as a mixture of methanol monomer, dimer, trimer, and tetramer in local equilibrium were used to derive the enthalpy and entropy for dimer and tetramer formation and these values agreed quite well with those of Weltner and Pitzer. In contrast, Tucker et al.16 found PVT measurements of vapor phase methanol were better fit by a monomer-trimer-octamer model than the usual monomer-dimer-tetramer assumption.

More direct evidence for clusters and their conformations comes from infrared or Raman spectroscopy measurements of clusters formed in supersonic expansions. 17-19 In some cases, clusters were size-selected and the vibrational bands assigned to specific i-mers. 4,11,20,21 The fact that the free OH peak observed for monomers and dimers does not show up for cluster sizes $n \ge 3$ suggests a cyclical structure with no unbonded H for larger clusters. 11,17,20 This is consistent with the behavior of clusters in molecular beam electric deflection, where the defocusing of clusters with $n \ge 3$ also indicates nonpolar ring structures.²² IR action spectra measurements¹³ find the hydrogen bonded OH stretch band shifts from 3473 cm⁻¹ for the trimer to 3300 cm⁻¹ for the tetramer, leveling off as the cluster size reaches the pentamer (3240 cm⁻¹) and hexamer (3210 cm⁻¹). Furthermore, the broadening of the OH stretch region indicates a cooperative effect as the cluster size increases, 13 i.e., the binding energy of the trimer is more negative than that predicted by the sum of two body interactions.²³ For clusters with sizes from 9 to 39, the OH vibrational band shows a single peak at a size-independent position, which suggests that the H-bond network maintains its ring-structure.21

Computational approaches inherently complement the experimental cluster studies. The density functional theory calculations of Boyd and Boyd²⁴ estimated dissociation energies and average O-H vibrational frequencies for methanol clusters up to i = 12 for a wide range of isomers.²⁴ They found that, in general, cluster dissociation energies converged to that expected for the bulk liquid by the pentamer or hexamer as did the average vibrational frequency.²⁴ Similarly, in *n*-layered integrated molecular orbital and molecular mechanics calculations, Pires and DeTuri7 found that cluster properties approached the bulk values for hexamers. More recently, Umer and Leonhard²⁵ used ab initio methods to determine the thermodynamic properties of clusters up to i = 6 at 298 K. They then incorporated the thermodynamic parameters into a gas phase cluster model and found that within the model's applicable range, the predicted gas phase densities were within 20% of the experimental values and, furthermore, that the dominant cluster size changed from the dimer to larger clusters with an increase in methanol partial

In vapor phase nucleation experiments, the P-T behavior of a dilute methanol-carrier gas mixture expanding isentropically can deviate from that of an ideal non-associating gas mixture as the equilibrium cluster concentrations adjust to the changing thermodynamic state of the vapor. As the cluster concentrations increase, the heat of association that is added to the expanding vapor perturbs the thermodynamic state of the flow and must be accounted for if the expansion trajectory is to be calculated correctly.

In the study of Laksmono et al. on methanol nucleation from a dilute vapor mixture flowing through a supersonic nozzle, 26 dimer and tetramer were assumed to be in equilibrium with vapor and condensed methanol under supercooled conditions. The data inversion procedure—based on static pressure and Tunable Diode Laser Absorption Spectroscopy (TDLAS) temperature measurements-predicted, however, that the liquid phase should appear well before liquid droplets were detected by small angle x-ray scattering (SAXS). This discrepancy suggested that clusters larger than the tetramer were present and that their presence should be incorporated into the model to properly account for the heat released to the flow prior to the appearance of liquid droplets.

The prediction of cluster formation is challenging in the temperature range required to condense methanol in our supersonic nozzle experiments due to the absence of available thermodynamic

data. Thus, the first goal of the paper is to use the results of Monte Carlo simulations to calculate the thermodynamic properties of larger methanol clusters so that these can be incorporated into an improved equilibrium model. The pressure and temperature data of Laksmono et al. 26 are then used to validate the approach and to determine the largest cluster size required to match the measurements prior to the appearance of the liquid. The second goal of this paper is to investigate the effect of water on methanol cluster formation and on the transition from pure methanol to binary methanol-water nucleation. We are particularly interested in observing whether particle formation is enhanced by the presence of precritical methanol clusters that are in equilibrium with the monomer.

The paper is organized as follows: In Sec. II, we describe the theory used to calculate the equilibrium clustering of pure methanol in the vapor phase. The experimental methods are summarized in Sec. III. In Sec. IV, the cluster model is first validated against the supersonic nozzle expansion data of Laksmono et al.26 and the results of experiments incorporating water over the whole concentration range are then presented and discussed. Section V summarizes our findings and conclusions. The supplementary material briefly summarizes the Monte Carlo method used to determine the thermodynamic cluster properties, the physical properties of methanol, water and their mixtures, and additional model verification results.

II. THERMODYNAMIC FORMALISM

A. Equilibrium i-mer concentrations

For a closed system consisting of an inert carrier gas and a vapor A forming small cluster species A_i containing i monomers (i-mers), the equilibrium association reactions take the form

$$iA = A_i. (1)$$

When the resulting gas phase species form an ideal gas mixture, their equilibrium concentrations may be determined from the wellknown mass action expressions. A convenient starting point is the pressure form of the law of mass action, which, for a reaction of the form of Eq. (1) reads

$$p_i = (p_1)^i \exp(-\Delta \mu_i^0 / kT) \equiv (p_1)^i K_i,$$
 (2)

where p_i is the partial pressure of species i, K_i is the pressure equilibrium constant, k is the Boltzmann constant, T is temperature, and $\Delta \mu_i^0$ is the standard state chemical potential difference for the *i*-mer formation reaction, Eq. (1),

$$\Delta \mu_i^0 = \mu_i^0 - i \mu_1^0. \tag{3}$$

Equation (2) may be rewritten in terms of the i-mer number densities, n_i , with the help of the ideal gas expression, $p_i = n_i kT$. The result is

$$n_i = (n_1)^i (kT)^{i-1} K_i \equiv (n_1)^i K_{ni},$$
 (4)

where K_{ni} is the number density equilibrium constant. The $\Delta \mu_i^0$ values needed to calculate the K_i may be available from experiments, or they may be determined by theoretical calculations or simulations.

The latter include Monte Carlo simulation results and Hale's statistical mechanical formalism presented elsewhere. ^{27–29} In terms of that formalism, the law of mass action is given as

$$N_i = N_1 \exp \left(-\sum_{j=2}^i \left[\delta f_j + \ln \left(n_\ell / n_1^e \right) - \ln S \right] \right), \tag{5}$$

where N_i and N_1 are, respectively, the number of *i*-mers and monomers in the system volume V, δf_j are dimensionless free energy differences obtained from the Monte Carlo simulations as explained in the supplementary material, n_ℓ is the number density of the liquid, n_i^e is the equilibrium monomer density, and S is the supersaturation, defined as $S = n_1/n_1^e$. Upon dividing both sides of Eq. (5) by V and rearranging the ln terms, we find the following expression for the number densities, $n_i = N_i/V$:

$$n_i = (n_1)^i \exp\left(-\sum_{j=2}^i \left[\delta f_j + \ln(n_\ell)\right]\right), \tag{6}$$

which can be compared with Eq. (4) to obtain the following result for the K_{ni} :

$$K_{ni} = n_{\ell}^{1-i} \exp\left(-\sum_{j=2}^{i} \delta f_j\right). \tag{7}$$

We see that K_{ni} , formally, has dimensions of (number density)¹⁻ⁱ. From Eq. (4), we also find the following expression for $K_{ni}(=K_i)$:

$$K_i = \left(n_{\ell}kT\right)^{1-i} \exp\left(-\sum_{j=2}^i \delta f_j\right),\tag{8}$$

which is seen to have formal dimensions of (pressure) $^{1-i}$.

We can use Eq. (8) to evaluate the standard state enthalpies Δh_i^0 and entropies Δs_i^0 of *i*-mer formation. To facilitate this, we introduce the standard state pressure p^0 and rewrite K_i as

$$K_i = \left(p^0\right)^{1-i} \exp\left(-\sum_{j=2}^i \left[\delta f_j + \ln\left(n_\ell k T/p^0\right)\right]\right). \tag{9}$$

Equation (9) has two useful features: First, the units of K_i can be adjusted simply by choosing the appropriate value of p^0 (e.g., 1 atm, $1.013\,25\times10^5$ Pa, etc.). Second, the argument in the ln term is now dimensionless and independent of the value chosen for p^0 . By comparing Eqs. (2) and (9), we can interpret $\Delta\mu_i^0$ in terms of the Monte Carlo results as

$$\frac{\Delta \mu_i^0}{kT} = \sum_{i=2}^i \left[\delta f_j + \ln \left(n_\ell kT/p^0 \right) \right]. \tag{10}$$

(The constant prefactor $(p^0)^{1-i}$ can be safely ignored. Normally, this term is hidden in conventional formulations of equilibrium constants.) This result enables us to evaluate Δh_i^0 with the well-known Gibbs–Helmholtz relation,

$$\frac{d}{dT} \left(\frac{\Delta \mu_i^0}{kT} \right) = -\frac{\Delta h_i^0}{T^2}.$$
 (11)

To implement this, it is best to take advantage of the scaled temperature dependence of δf_i ,

$$\delta f_j = \delta f_j^{sc} \left(\frac{T_c}{T} - 1 \right), \tag{12}$$

where δf_j^{sc} are temperature independent dimensionless constants and T_c is the critical temperature. The efficacy of the scaling approach is well illustrated in previously published work. ^{27–29} We then obtain

$$\Delta h_i^0 = \sum_{i=2}^{i} \left[k T_c \delta f_j^{sc} - k T (1 + T d \ln n_\ell / dT) \right], \tag{13}$$

from Eqs. (10)–(12). Since the liquid density is only weakly dependent on T, the contribution of the thermal expansivity term is modest, $Td\ln n_\ell/dT \approx 0.3$ at 250 K. In our case, it does not contribute at all because a constant value of n_ℓ was used simply to determine an appropriate volume scale for the simulations. In this case, we obtain the simpler result

$$\Delta h_i^0 = kT_c \sum_{j=2}^{i} \delta f_j^{sc} - (i-1)kT.$$
 (14)

The Δs_i^0 may be obtained by subtraction $(\Delta \mu_i^0 = \Delta h_i^0 - T \Delta s_i^0)$ or by differentiation $(\Delta s_i^0 = d\Delta \mu_i^0/dT)$. Either way, we find

$$\Delta s_i^0 = k \sum_{i=2}^{i} \left[\delta f_j^{sc} - \left(1 + \ln(n_{\ell} k T / p^0) \right) \right], \tag{15}$$

where n_{ℓ} has again been held constant.

B. Equilibrium constants

Equilibrium constants based solely on MC results are straight-forward to compute using Eqs. (7) and (9). The problem with this approach is that the dimer and tetramer values do not compare well with experimental values. At 240 K, they are roughly two times higher than the K_2 value and two times lower than the K_4 value reported by Weltner and Pitzer. To improve the situation, we therefore use the experimental values of Δh_i^0 and Δs_i^0 to determine the dimer and tetramer equilibrium constants and then use the MC values to determine values for the trimers and all *i*-mers larger than tetramers. The underlying assumption is that although the absolute MC free energies for the *i*-mers may not be accurate, the differences between successive cluster sizes should be reasonable.

The approach to blend the two datasets is first illustrated for K_3 . Here, we write

$$K_3 = (p^0)^{-2} \exp(-\Delta \mu_3^0 / kT),$$
 (16)

where $\Delta \mu_3^0$ is expressed as

$$\Delta \mu_3^0 = \Delta \mu_2^0 + (\Delta \mu_3^0 - \Delta \mu_2^0)_{MC}. \tag{17}$$

The subscript MC on the free energy difference indicates that this term is to be evaluated using the Monte Carlo results in Eq. (10),

TABLE I. Mean values of scaled MC free energy differences δf^{sc}

i	$-\delta f_i^{sc}$	i	$-\delta f_i^{sc}$
2	4.19	8	8.64
3	7.59	9	8.56
4	11.4	10	8.90
5	9.46	11	8.65
6	8.14	12	9.11
7	8.39		

while $\Delta \mu_2^0$ is evaluated using the experimental values of Weltner and Pitzer for Δh_2^0 and Δs_2^0 . This yields the following expression for K_3 :

$$K_3 = (n_{\ell}kT)^{-1}K_2 \exp(-\delta f_3^{sc}[(T_C/T) - 1]),$$
 (18)

where

$$K_2 = (p^0)^{-1} \exp(-[\Delta h_2^0 - T\Delta s_2^0]/kT).$$
 (19)

The experimental values of K_4 can also be used as a base for estimating K_3 , and for this choice, the values are 2–3 times larger than those using K_2 . Most previous works have found that trimer concentrations are insignificant relative to that of the dimer or tetramer. Thus, we prefer to use the smaller values of K_3 . For *i*-mers larger than the tetramer, we use K_4 as the base. The calculation for K_5 is as follows:

$$K_5 = (n_{\ell}kT)^{-1}K_4 \exp(-\delta f_5^{sc}[(T_C/T) - 1]),$$
 (20)

where $K_4 = (p^0)^{-3} \exp(-[\Delta h_4^0 - T \Delta s_4^0]/kT)$ and the values for Δh_4^0 and Δs_4^0 are taken from the work of Weltner and Pitzer. For the higher *i*-mers, the K_i values are found using the simple recursion formula

$$K_i = (n_{\ell}kT)^{-1}K_{i-1} \exp(-\delta f_i^{sc}[(T_C/T) - 1]).$$
 (21)

For clusters other than dimers and tetramers, the values of Δh_i^0 and Δs_i^0 can be written as

$$\Delta h_i^0 = \Delta h_{i-1}^0 + k \left[T_C \delta f_i^{sc} - T \right]$$
 (22)

and

$$\Delta s_i^0 = \Delta s_{i-1}^0 + k \left[\delta f_i^{sc} - \left(1 + \ln \left(n_{\ell} k T / p^0 \right) \right) \right]. \tag{23}$$

The δf_i^{SC} values are summarized in Table I. The hybrid K(i) values determined here are first used in a code that models the cluster concentrations and heat release in methanol vapor undergoing isentropic expansion. They are then incorporated into the data inversion program used to interpret the pressure traces of the unary and binary nucleation experiments.

III. EXPERIMENTAL

The experimental apparatus uses the flow system detailed in the work of Laksmono *et al.*²⁶ but with the FTIR configuration outlined in the work of Park and Wyslouzil.³⁰ The supersonic nozzle is

assembled from two 1.27 cm wide aluminum blocks that define the converging–diverging shape (top and bottom) and two flat sidewalls that enclose the flow. Each sidewall has a CaF₂ window for optical access. At the nozzle entrance, the cross section is constant for ~2 cm and the static pressure measured here is corrected for the kinetic energy of the flow to determine the true stagnation pressure p_0 . The shaped portion of the nozzle consists of a ~4 cm long converging region and a ~12 cm long diverging region. At the narrowest point, corresponding to the nozzle throat, the flow channel has a height of 0.5 cm. The expansion rate in the diverging section is $d(A/A^*)/dz = 0.043 \text{ cm}^{-1}$, which provides cooling rates that decrease from ~8 × 10⁵ K/s near the throat to ~1 × 10⁵ K/s further downstream. Here, A is the cross-sectional area at position z (cm) and A^* is the area of the nozzle throat.

During the experiments, \sim 17 mol/min carrier gas is drawn from the boil-off of three high pressure liquid nitrogen Dewars. After the cold nitrogen gas is heated, it flows to the water bath where the stagnation temperature T_0 is reached. This temperature is measured in the plenum by a platinum resistance temperature detector just before the gas enters the nozzle. In the experiments conducted at constant methanol partial pressure, methanol and water are pumped into the system by separate peristaltic pumps, vaporized by heating, and dispersed into the flowing nitrogen. In the remaining experiments, methanol and water are first mixed, allowed to equilibrate for at least 1 h, pumped into the system using a single peristaltic pump, and vaporized before entering the flow.

A. Pressure trace measurements

A movable pressure probe mounted in the nozzle measures the axial static pressure profile along the centerline of the flow in an experiment we refer to as a pressure trace measurement (PTM). The flow is assumed to be one-dimensional since the expansion is quite gentle. When the pure carrier gas (nitrogen) flows through the nozzle (dry trace), the pressure and temperature follow isentropic expansion profiles. Temperature T, flow density ρ , velocity u, and cross-sectional area ratio A/A^* can be calculated from the measured static pressure p by simultaneously solving the continuity equation, an equation of state, and momentum and energy balance. When the condensable carrier gas mixture flows through the nozzle (wet trace), the gas mixture first follows the expected isentropic expansion. When methanol cluster and/or liquid forms, the heat released to the flow raises both the temperature and static pressure relative to the expected isentropic flow. If we assume that heat release does not change the area ratio profile relative to the dry trace, the other relevant properties can be calculated by solving the four equations noted above using pressure and area ratio as input. Prior to heat release, this is a good assumption, but as heat is released to the flow, the boundary layers that develop along the nozzle wall are slightly compressed relative to the dry flow. 31 Thus, the area ratio in the presence of clustering or condensation is slightly larger than that expected based on the isentropic expansion and the temperature is underestimated. The approach used in this paper to correct for this effect is described in Sec. IV B.

All expansions started from a stagnation pressure $p_0 = 60.00 \pm 0.03$ kPa and initial temperature of $T_0 = 318.0 \pm 0.1$ or 308.2 ± 0.1 K. For pure methanol experiments, the partial pressure varied in the range 0.5 kPa $\leq p_{v0,methanol} \leq 1.7$ kPa. In some of the binary experiments the methanol partial pressure was held constant

at $p_{v0, \text{methanol}} = 1.3$ kPa, and low amounts of water were added to the system to yield water mol percentages x_{water} ranging from 3 to 24 mol %. The water mol percentage is defined as $x_{\text{water}} = n_{\text{water}}/(n_{\text{water}} + n_{\text{methanol}}) \times 100\%$ where n_{water} (n_{methanol}) is the molar flow rate of water (methanol) entering the system. In the experiments where both methanol and water vapor pressure varied at a constant value of x_{water} the two species were mixed in advance and flow rates were varied to span the range of desired onset temperatures.

In most vapor phase nucleation studies under our experimental conditions, i-mer concentrations are very low compared to those of the monomer and liquid and all heat released to the flow is attributed to liquid formation. In contrast, for nucleation of pure methanol or under methanol-rich conditions, clustering cannot be ignored and needs to be incorporated into the data inversion program to correctly predict the distribution of methanol between clusters and nanometer-sized liquid droplets. In the current work, the data inversion code includes clusters up to a maximum size $i_{\rm max}$. These clusters are assumed to be in equilibrium with the monomer and the equilibrium constants calculated using the hybrid approach described in Sec. II. The equations used to incorporate cluster formation into the data analysis code and to attribute the heat release to clusters and/or liquid methanol formation are detailed in the Appendix of Laksmono $et\ al.^{26}$

Finally, methanol and water have different vapor pressures and form nonideal mixtures. Thus, the composition of the condensed phase will differ from that of the vapor. When both species are present in the condensed phase, the code assumes that the vapors and carrier gas form an ideal gas mixture and that the equilibrium vapor phase partial pressures $p_{\rm vi}$ are related to the liquid composition via

$$\frac{p_{v1}}{p_{v2}} = \frac{p_{e1}x_1\gamma_1}{p_{e2}x_2\gamma_2},$$
(24)

where p_{ei} is the equilibrium vapor pressure of the pure species i, x_i is the mole fraction of i in the condensed phase, assuming a uniform distribution of i throughout the droplet, and γ_i is the liquid activity coefficient of species i. Nonideality is described by the two-suffix Margules equations (as documented in the supplementary material).

B. FTIR

In the FTIR measurements, absorption spectra are taken every 0.35 cm downstream of the nozzle throat. For each spectrum, 32 scans are made over the wavenumber range $4000-900~{\rm cm}^{-1}$ with resolution of 1 cm $^{-1}$. Since the IR beam path is not purged, the CO₂/H₂O suppression software is used to minimize the absorption from these species in the surrounding air. At each position, a background spectrum (carrier gas only) is measured first, followed by the sample (nitrogen + condensable species) measurement, and the resultant transmission spectrum is calculated. To determine the methanol monomer concentration from the transmission spectrum, the intensity in the free OH absorption region (3800–3600 cm $^{-1}$) is first scaled to account for the decreasing density of the expanding flow. Any additional scaling required to match the absorption in the absence of clustering reflects methanol monomer consumption due to clustering or condensation.

C. Chemicals

Liquid nitrogen (purity of 99.998%) was purchased from Praxair, Inc. The deionized water had a resistivity of ~18 M Ω . Methanol

(purity ≥99.9%) was purchased from Sigma–Aldrich. The thermodynamic properties of the pure components and their mixtures are summarized in Sec. II of the supplementary material (Tables S1 and S2, Figs. S1 and S2).

IV. RESULTS AND DISCUSSIONS

A. Cluster model validation

In the work of Laksmono *et al.*, ²⁶ methanol vapor was assumed to be in equilibrium with dimers and tetramers. Since the formation of these *i*-mers did not release enough heat to the flow to account for the changes in pressure and temperature observed in the experiment, the data analysis code predicted the presence of liquid well before it was observed in complementary small angle x-ray scattering experiments. This discrepancy was attributed to the presence of larger clusters that were not accounted for in the nozzle flow model. The question remains: what is the largest cluster size required in the model to account for the heat release during polymerization of methanol under those or similar experimental conditions?

To answer this question, we used the equilibrium constants derived in Sec. II of this paper in a simple model that predicts the temperature–pressure behavior of an isentropic expansion in which the methanol monomer is in local equilibrium with the i-mers up to a selected cluster size $i_{\rm max}$. The starting stagnation temperatures, pressures, and partial pressures of methanol correspond to the measurements reported by Laksmono $et\ al.^{26}$ Only the data in the range prior to the appearance of liquid, as detected by the small angle x-ray scattering measurements, were considered. We note that because Laksmono $et\ al.$ measured both pressure and temperature, the area ratio of the flow was determined as part of the data inversion process. Downstream of the initiation of heat addition, the area ratio was generally ~1%–2% higher than the corresponding value of the dry flow due to mild compression of the boundary layers. 31

The results are illustrated in Figs. 1 and 2 for the highest methanol partial pressure. As shown in Fig. 1(a), there is no discernible difference between $i_{max} = 2$ (or $i_{max} = 3$, not shown) and the expansion based on $i_{\max}=1$, i.e., the expansion calculated using the ideal heat capacity C_p^0 of methanol. Prior to the appearance of the liquid at p = 16.3 kPa, the equilibrium temperature increases significantly when i_{max} is increased to 4 and again from 4 to 5, leveling off when i_{max} is in the range of 6–12. When $i_{\text{max}} = 6$, the temperature corresponding to p = 16.3 kPa is ~223.4 K, and T only increases by ~ 0.4 K when i_{max} is increased from 6 to 12. Both values compare favorably with the reported experimental temperature 224.7 \pm 2 K. These results are summarized in Fig. 1(b). The inclusion of trimers does not change the equilibrium temperature from that observed for the dimer since the trimer concentration is generally less than ~50% of the dimer concentration. Using the Δh_4^0 and Δs_4^0 values of Renner et al. 15 results in temperatures that are ~2 K lower for $i \ge 4$. Based on these results, using $i_{max} = 6$ and blending the MC results with the experimental values of Weltner and Pitzer,14 a model that is considered a good trade-off between the accuracy of the results and ease of calculation is obtained.

The corresponding concentration profiles for the clusters when $i_{\rm max}=6$, Fig. 2, show that the pentamer rapidly overtakes the tetramer as the dominant species and remains higher than the hexamer down to the temperatures and pressures achieved in these

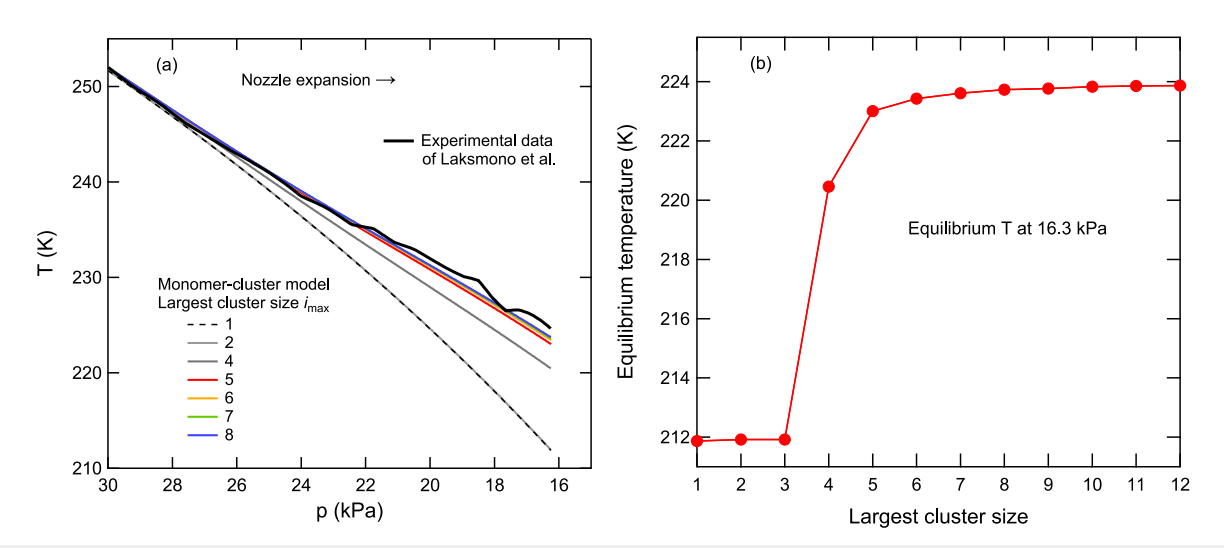


FIG. 1. (a) The temperature–pressure relationship measured for the expanding gas mixture is compared to those calculated for isentropic expansions using a model that assumes monomer–cluster equilibrium for different values of i_{max} . The equilibrium constants are derived as described in Sec. II, and calculations start from the experimental stagnation conditions: $p_0 = 59.6 \text{ kPa}$, $T_0 = 305 \text{ K}$, and $p_{v0,\text{methanol}} = 2.09 \text{ kPa}$. The expansion with $i_{\text{max}} = 1$ (dashed black curve) essentially overlaps the $i_{\text{max}} = 2$ case (solid gray curve). As i_{max} increases up to $i_{\text{max}} = 12$, the equilibrium temperature approaches the experimentally measured value. (b) When the gas mixture (nitrogen + methanol) expands from p_0 to 16.3 kPa, the predicted equilibrium temperature increases with the size of the largest cluster included in the monomer–cluster model. The predicted temperature begins to level off when clusters larger than pentamer are incorporated and approaches the experimentally measured temperature of 224.7 K. When clusters up to hexamer are included, the calculated temperature is 223.4 K, which is well within the overall experimental error of ± 2 K.

experiments. As illustrated in Fig. S3 for the lower initial methanol partial pressures, setting $i_{\rm max}=6$ also captures the temperature rise of the flow quite well despite the lower flow temperatures. These results are consistent with the estimate reported by Laksmono *et al.*, ²⁶

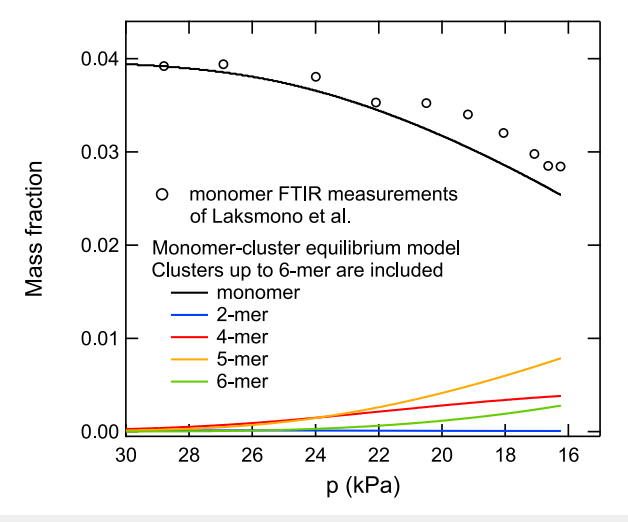


FIG. 2. Monomer and cluster mass fractions predicted by the model for $i_{\rm max}=6$. The initial mass fraction of the monomer with respect to the gas mixture (nitrogen and methanol) is 0.039 88. As the expansion proceeds monomers form clusters and are depleted from the gas phase. Prior to the appearance of the liquid, cluster formation consumes ~36% of the initial monomer. The measured monomer fraction, determined from the free OH band in the IR spectra, is ~7% higher than the values calculated using the monomer–cluster equilibrium model, a discrepancy largely explained by boundary layer effects (see main text).

based on small angle x-ray scattering, that the peak in the cluster distribution was at i = 6.

Figure 2 also compares the predicted mass fraction of methanol monomer as a function of pressure to the experimental measurements. In the cluster formation region—where the pressure drops from about 30 to 16.3 kPa—the measured monomer mass fraction is about 7% higher than that calculated by the monomer-cluster equilibrium calculation. This discrepancy is largely consistent with the presence of the boundary layers that develop along the walls of the nozzle during the expansion. Although the gas mixture in the boundary layers is at the same pressure as the core flow, the temperature increases across the boundary layer to approach the recovery temperature at the walls. In the IR measurements, the measured free OH band intensity is used to determine the mass fraction of monomer. The beam, however, probes the whole cross-sectional area of the nozzle, including the boundary layer; thus, the free OH signal not only comes from the core of the flow but also contains contributions from the monomers in the boundary layer that do not associate to form clusters because of the higher temperature. At a point 4 cm downstream of the throat, the boundary layer thickness is estimated to be 0.1 mm and to comprise about 5% of the total cross-sectional area. Even though this does not completely explain the difference between the measured monomer concentration from the FTIR and that calculated from the monomer-cluster equilibrium, it does suggest that the boundary layer introduces a systematic offset between the monomer estimates derived from direct FTIR and the combined pressure/temperature measurements.

B. Pure methanol condensation

Based on the model validation, including the dimer, tetramer, pentamer, and hexamer adequately accounts for the observed heat

release due to clustering in the case of gently expanding nozzle reported by Laksmono et al. Since the current experiments access a similar range of temperatures and methanol partial pressures in a comparable nozzle, this model should also describe the current data during methanol and methanol-water nucleation. Simply including clusters up to the 6-mer in the flow analysis model without accounting for small changes in the area ratio due to compression of the boundary layer upon heat addition, however, can yield significant negative liquid mass fractions prior to particle formation (Fig. S4). This is because the flow temperature is underestimated when it is determined using the wet pressure measurement and the area ratio for the dry pressure trace.³¹ Thus, the model produces overly high cluster concentrations, the heat input is too high, and the data inversion code generates "negative (unphysical) liquid" mass fractions in order to balance the energy and the total amount of methanol. This result is clearly not physical and simply indicates that it is necessary to include a small (<~1.5%) correction to the area ratio. Based on the differences between $(A/A^*)_{dry}$ and $(A/A^*)_{wet}$ observed by Laksmono et al., we make this correction by introducing a factor k (k < 0.01) and adjusting the area ratio at position zas $(A/A^*)_{\text{wet}} = (A/A^*)_{\text{dry}} + k \times (z - z_1)/(z_2 - z_1)$. Here, z_1 is the position where the pressure trace first deviates from the expected isentropic expansion due to heat addition from clustering and z_2 is the end of the nozzle. The value of k is chosen so that (1) liquid mass fraction is close to zero prior to particle formation and (2) the predicted monomer concentrations are close to but below those determined using FTIR measurements of the free OH band.

The resultant pressure ratio, temperature, and mass fraction profiles for the $p_{v0,methanol} = 1.3$ kPa experiment are shown in Fig. 3. Cluster formation starts ~1.9 cm downstream of the throat, whereas droplets start to constitute a significant fraction of the condensed mass close to $z \sim 7$ cm. Figure 3(b) shows the predicted mass

fractions of the methanol monomer and the selected i-mers assuming $i_{\text{max}} = 6$. Clusters reach their maximum concentrations right before rapid droplet growth ensues; they then dissociate as the temperature rises and equilibrium concentrations decrease. Pentamers dominate, and dimers play almost no role. The mass fraction of liquid between 2 and 7 cm is forced to be close to zero by choosing k = 0.008 to correct for boundary layer compression. This choice is consistent with the pure methanol data reported in the work of Laksmono et al., where $(A/A^*)_{wet}$ was about 1% (2%) larger than $(A/A^*)_{dry}$ before (after) particle formation. About 50% of the methanol monomers are consumed near the end of the nozzle.

Figure 3(b) also compares the predicted monomer concentration to that measured using FTIR data. The latter is determined by analyzing the absorption stemming from the free OH of the methanol monomer¹² in the region of 3800-3600 cm⁻¹, and typical spectra corresponding to $p_{v0,methanol} = 1.3$ kPa are illustrated in Fig. 4. Even though methanol dimers also absorb in this region,²⁰ their absorbance is expected to be negligible because in our case their concentration is always significantly lower than that of the

In these expanding flows, the absorption intensity decreases both due to the decreasing density of the flow and due to the consumption of monomer by clustering and particle formation. The first step in analyzing the FTIR data is, therefore, to choose a reference position far enough upstream to ensure that clustering is effectively zero. Here, we choose z = 0.35 cm because at this position, the wet pressure trace overlaps that of the expected isentropic expansion and the signal in the H-bonded OH stretch region (3600-3000 cm⁻¹) matches the baseline, indicating that essentially no clustering has occurred. Thus, at z = 0.35 cm, g of the monomer equals g of the initial gas mixture. Further downstream, the mass fraction of the monomer at position z is calculated as

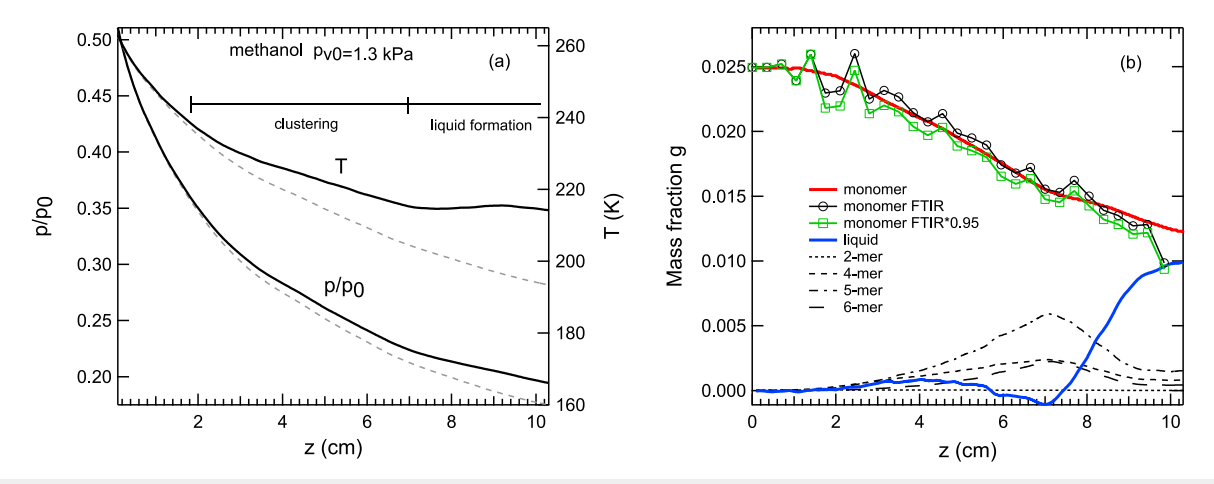
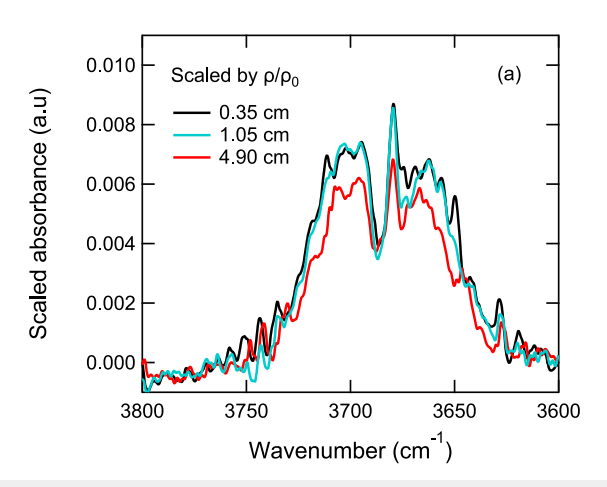


FIG. 3. (a) Pressure and temperature profiles downstream of the nozzle throat (z=0) for $p_{V0,methanol}=1.3$ kPa. The gentle deviations of T and p from the expected isentropic expansion (dashed lines) start near $z\sim1.9$ cm and reflect heat release due to cluster formation. The more rapid deviations of T and p that start near T0 cm correspond to droplet formation. (b) The mass fractions of the monomer, clusters, and liquid (lines) are calculated from the PTM using a data inversion code that accounts for the presence of subcritical clusters in equilibrium with the monomer. Cluster concentrations are predicted to reach a maximum just prior to particle formation. The area ratio was adjusted using k = 0.008 to correct for boundary layer compression (see main text) and to ensure that liquid concentration is close to zero for z < -7 cm. At the nozzle exit, ~50% of the methanol monomer has condensed. The green (black) symbols indicate the methanol monomer mass fractions determined by FTIR measurements after (before) accounting for the presence of the boundary layers.



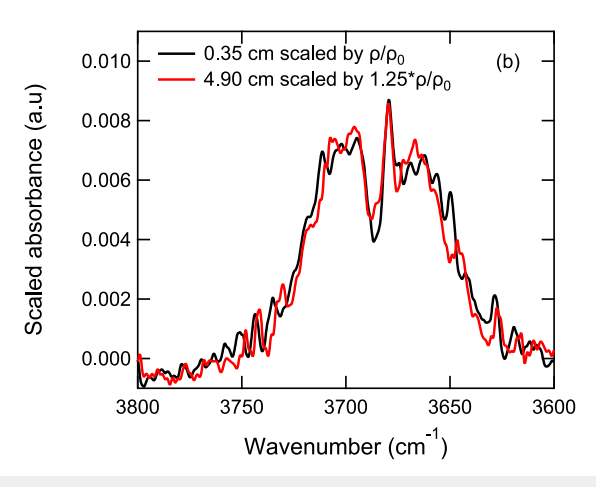


FIG. 4. Free OH band in the region of 3800– $3600~\text{cm}^{-1}$. (a) The raw spectra are scaled by dividing by the density ratio ρ/ρ_0 , where ρ_0 is the density of the initial gas mixture, to compensate for expansion of the flow. The scaled spectra at z=0.35~cm and z=1.05~cm overlap quite well because significant clustering has not yet started, and methanol exists primarily as the monomer. The scaled intensity at z=4.90~cm is lower since the monomers are partially consumed by cluster formation. (b) To derive the mass fraction of monomer at 4.90 cm, the scaling factor is determined by using a least square fit to minimize the difference between the scaled spectra at z=4.90~cm and z=0.35~cm. When SF=1.25, the two spectra match quite well in shape and intensity.

$$g_{\text{mon}}(z) = \frac{g_{\text{mon}}(0.35)}{SF(z)} \times \frac{\rho(0.35)}{\rho(z)},$$
 (25)

where SF(z) is the scaling factor required to match the baseline corrected raw spectrum measured at position z to that measured at z=0.35 cm. As illustrated in Fig. 4(a), after applying the appropriate density corrections, the spectrum measured at z=1.05 cm matches the reference spectrum, i.e., $SF(1.05) = \frac{\rho(0.35)}{\rho(1.05)}$ and $g_{\text{mon}}(1.05) = g_{\text{mon}}(0.35)$. In contrast, the spectrum measured at z=4.9 cm, Fig. 4(b), only matches the reference spectrum when $SF(4.9) = 1.25 \times \frac{\rho(0.35)}{\rho(4.90)}$ and $g_{\text{mon}}(4.9) = \frac{g_{\text{mon}}(0.35)}{1.25}$. These results are consistent with the pressure measurements where heat release is not evident at z=1.05 cm but is clearly evident at z=4.9 cm.

Finally, as discussed in Sec. III A, the IR beam probes the entire flow and includes contributions from monomer present in the higher temperature boundary layers, whereas analysis of the PTM characterizes only the core flow. Based on our estimates for the boundary layer thickness of the current nozzle, this difference should result in ~5% higher monomer concentrations measured via FTIR spectroscopy. The boundary layer thickness in the current nozzle is somewhat less than that in the case reported by Laksmono *et al.* because the nozzle used in the current study expands slightly less rapidly than theirs. After applying a 5% correction, the results of the two characterization methods illustrated in Fig. 3(b) agree quite well.

C. Methanol-water nucleation

To investigate the role of clustering in binary condensation, we conducted experiments ranging from pure methanol to pure water with particular emphasis on exploring the transition from pure methanol nucleation to binary nucleation. In the limit of low water vapor concentrations, two key questions are (1) whether the addition of water changes methanol clustering significantly prior to the appearance of the liquid phase, and (2) what level of water is

required for binary particle formation to occur at temperatures high enough to preclude significant methanol clustering from occurring. Methanol and water binary condensation experiments were therefore conducted with a constant initial methanol vapor pressure of 1.3 kPa and varying initial water vapor pressures.

The pressure and temperature profiles determined for these experiments are illustrated in Fig. 5. For the methanol-water cases, the initial deviations of pressure and temperature from the isentropic expansions overlap those of the pure methanol case remarkably well. One interpretation of this is that the presence of water does not significantly interfere with methanol cluster formation under our experimental conditions. At the lowest water concentration (3 mol %), pure methanol clusters should dominate simply because methanol monomers outnumber water monomers by a factor of 30. Even if the mixed clusters form, the results reported in the work of Umer and Leonhard²⁵ suggest that the heat released by the formation of a mixed cluster should be very close to that for a pure methanol cluster. What does change dramatically is the temperature at which the liquid forms. When water increases from 0 to 3 mol % of the total condensable, for example, condensation onset moves from 215 to 225 K. Once liquid formation starts, the increased heat release seen in Fig. 5 is consistent with the co-condensation of both species. Finally, at 24 mol % water, co-condensation starts at about the same temperature for which significant methanol clustering should start to be observed and, thus, the latter process no longer competes for methanol with binary particle formation. In contrast, in a limited series of methanol-octane condensation experiments (Fig. S5), particle formation is not promoted by the presence of the alkane even though octane has a much lower equilibrium vapor pressure than methanol or water and the octane supersaturation reaches 48 at 20 mol % octane. Although the temperature at onset does change slightly (<2 K), the increase in temperature is mainly due to the decreased heat capacity ratio of the gas mixture upon octane addition and the resulting slower expansion. Slower expansions probe

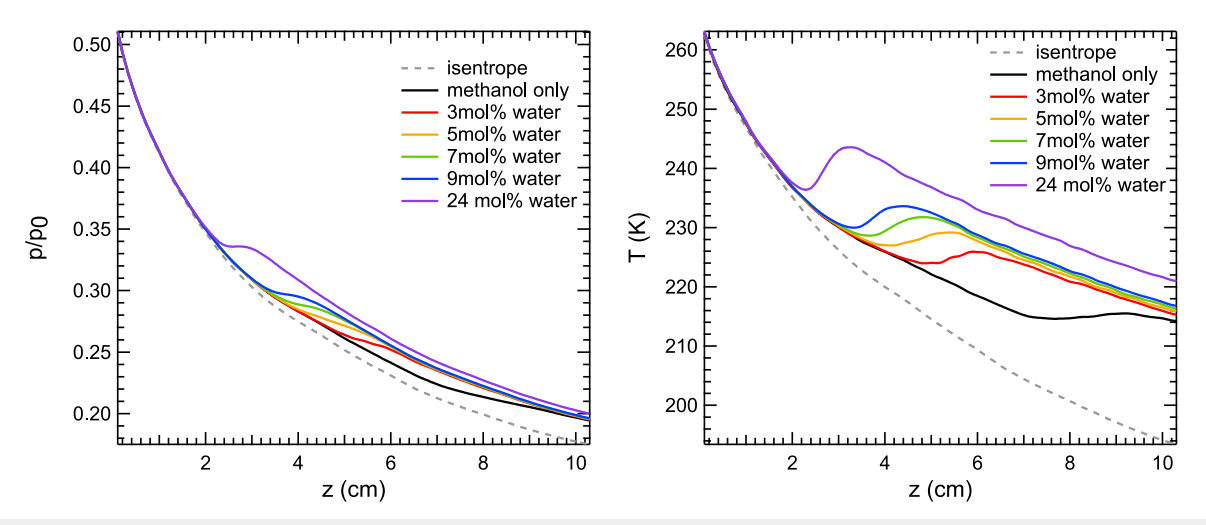


FIG. 5. Pressure ratio and temperature profiles for methanol—water nucleation at a fixed initial methanol partial pressure equal to 1.3 kPa. The mol % water—with respect to the total condensable material (methanol + water)—is indicated in the figure. As water is added to methanol, the temperatures and pressures in the cluster formation region (the gentle temperature deviation relative to the isentrope) are not visibly perturbed from the pure methanol curve. However, the droplets form earlier at higher temperature as indicated by the more rapid temperature increase.

the metastable region less deeply, i.e., the temperature associated with the phase transition is higher.

For completeness, binary nucleation experiments were then performed over the whole concentration range of water (0–100 mol %), and the conditions corresponding to the maximum nucleation rates, or onset, were determined. To our knowledge, the current measurements are the first condensation experiments involving methanol-water nucleation in expanding flows. The only other binary nucleation measurements for this system are the diffusion cloud chamber experiments of Flageollet et al. 32 Due to COVID restrictions, we were unable to characterize the aerosol using SAXS—a necessary step in determining actual nucleation rates.³ Extensive nucleation rate measurements for pure methanol,³⁶ pure water,³⁷ and ethanol-water³⁸ in comparable nozzles, however, show that these rates are always $10^{17\pm1}$ cm⁻³ s⁻¹, and there is no reason apriori to expect otherwise here. For methanol-water mixtures, onset is identified as the position where the activity of methanol $\frac{p_{v,methanol}}{p_{e,methanol}}$ is maximized. Since the equilibrium vapor pressures p_a decrease as an exponential function of temperature, onset is reached just before rapid droplet growth adds significant amounts of heat to the flow. The experimental initial conditions and onset conditions are summarized in Table II.

The total condensable partial pressures at onset ($p_{\text{on,methanol}}$ + $p_{\text{on, water}}$) are plotted as a function of temperature in Fig. 6. For pure methanol, the difference between the open black circles in Fig. 6(a) and the filled black circles emphasizes the importance of incorporating the presence of clusters and boundary layer corrections into the data inversion process. In the absence of these corrections, the onset pressure is overestimated because no monomers convert to clusters (1 to n conversion) and all heat release is attributed to liquid formation (1–1 conversion). The onset temperature is also underestimated because the effective expansion is assumed to be the same as the dry trace, but heat release is

known to increase the $d(A/A^*)/dz$ by ~ 1%–2 % in comparable experiments.

As the water concentration increases [Fig. 6(a)], the onset conditions for each fixed water concentration lie on roughly parallel lines progressively shifted toward higher temperature away from the pure methanol onset line. At a fixed onset temperature, the total onset pressure decreases as the water concentration increases. These trends continue to about 40 mol % water.

After the water concentration reaches about 24 mol %, clustering is negligible and the deviation of the condensing flow curves from the expected isentropic expansion is almost completely due to binary particle formation and growth rather than pure methanol clustering. The onset conditions between 40 mol % water and 60 mol % water [Fig. 6(b)] lie very close to each other, suggesting that in this range of compositions, onset only depends on the total pressure of the condensable and not by the composition of the mixture. As the water concentration continues to increase, the onset curves shift back toward the pure water line. The rapid decrease in pressure required to nucleate particles in the water-rich region on the addition of alcohol is consistent with the rapid decrease in surface tension associated with incorporating these amphiphilic alcohol molecules into the critical cluster.

We used the measured onset pressures of these methanol-water mixtures shown in Fig. 6 to estimate onset pressures at 220 K. These results are shown in Fig. 7(a). For highly ideal systems, for example, $H_2O-D_2O_3^{99}$ an isothermal $p_{v1}-p_{v2}$ plot varies linearly between the two species. The concave shape of the methanol-water curve observed here is consistent with a strong mutual enhancement of nucleation induced by the presence of the second species that is evident in other alcohol-water nucleation experiments. In the methanol-rich region, the onset conditions that ignore clustering and boundary layer corrections lie distinctly above the corrected

TABLE II. Experimental stagnation and onset conditions for methanol–water nucleation.

Stagnation condition			Onset condition			
p ₀ (kPa)	T ₀ (K)	Pv0,methanol (kPa)	p _{v0,water} (kPa)	T _{on} (K)	pon,methanol (Pa)	p _{on,water} (Pa)
			0 mol % wat	er		
59.98	308.2	0.489		200.3	47.9	
60.03	308.2	0.752		207.3	90.3	
60.06	318.1	1.105		211.5	134.9	• • •
60.04	308.2	1.015		212.2	140.3	
60.03	317.8	1.313	• • •	214.9	179.1	• • • •
60.04	318.0	1.661	•••	217.9	231.1	•••
			2 mol % wat	er		
60.02	317.9	0.625	0.014	210.2	99.1	2.7
60.01	318.0	1.453	0.032	222.8	288.2	6.8
60.00	318.0	1.877	0.041	226.7	392.4	9.1
			5 mol % wat	er		
59.93	318.0	0.409	0.022	207.7	70.6	4.3
60.02	318.1	0.636	0.035	214.2	124.3	6.8
60.01	318.0	1.040	0.057	222.3	237.4	12.5
60.02	318.0	1.356	0.074	226.4	326.1	16.4
			10 mol % wa	ter		
59.98	318.1	0.649	0.073	218.9	152.3	14.6
59.96	318.1	0.952	0.106	224.9	248.2	26.1
60.02	318.1	1.244	0.139	229.2	345.2	36.1
			24 mol % wa	ter		
59.98	318.1	0.287	0.091	210.7	62.0	14.8
59.98	318.0	0.554	0.176	221.9	148.1	43.0
59.97	317.9	0.905	0.288	230.3	275.5	81.1
60.00	317.9	1.095	0.348	233.6	351.1	105.9
			40 mol % wa	ter		
59.95	318.1	0.246	0.163	213.6	57.9	30.9
60.01	318.0	0.489	0.325	225.3	140.5	85.1
60.02	318.0	0.695	0.462	231.3	219.4	137.6
60.03	318.0	0.895	0.594	235.6	302.5	194.6
			50 mol % wa	ter		
60.00	318.1	0.235	0.235	216.0	58.5	51.7
60.03	318.0	0.497	0.497	228.9	152.5	143.7
60.04	318.0	0.755	0.755	236.2	257.0	245.0
			60 mol % wa	ter		
59.92	318.0	0.164	0.245	213.5	39.7	55.2
59.96	318.0	0.378	0.568	227.7	114.4	163.6
59.98	318.1	0.537	0.806	233.9	178.1	257.5

TABLE II. (Continued.)

Stagnation condition				Onset condition		
p ₀ (kPa)	T ₀ (K)	p _{v0,methanol} (kPa)	pv0,water (kPa)	T _{on} (K)	p _{on,methanol} (Pa)	pon,water (Pa)
			70 mol % wa	ter		
59.97	318.0	0.132	0.309	213.6	32.0	67.2
59.96	318.0	0.262	0.611	225.3	76.5	169.2
59.97	318.0	0.389	0.908	232.9	126.3	279.1
			80 mol % wa	ter		
59.98	318.0	0.116	0.465	217.2	30.0	113.2
60.04	317.9	0.142	0.567	220.6	38.6	146.6
60.00	317.9	0.177	0.707	224.1	51.3	200.5
			90 mol % wa	ter		
60.01	318.0	0.053	0.473	213.7	12.7	102.7
59.96	318.0	0.078	0.705	220.5	21.4	186.1
60.02	318.0	0.108	0.972	226.0	32.1	281.4
60.03	318.0	0.119	1.070	228.1	36.3	314.3
			100 mol % wa	iter		
59.98	308.2		0.406	207.4		93.6
60.03	308.2		0.608	214.9		164.2
60.00	317.9		0.744	216.7		187.9
60.01	318.0		0.889	219.7		234.9
60.00	317.9		1.061	223.0		295.7
59.94	317.9		1.267	226.6		373.5

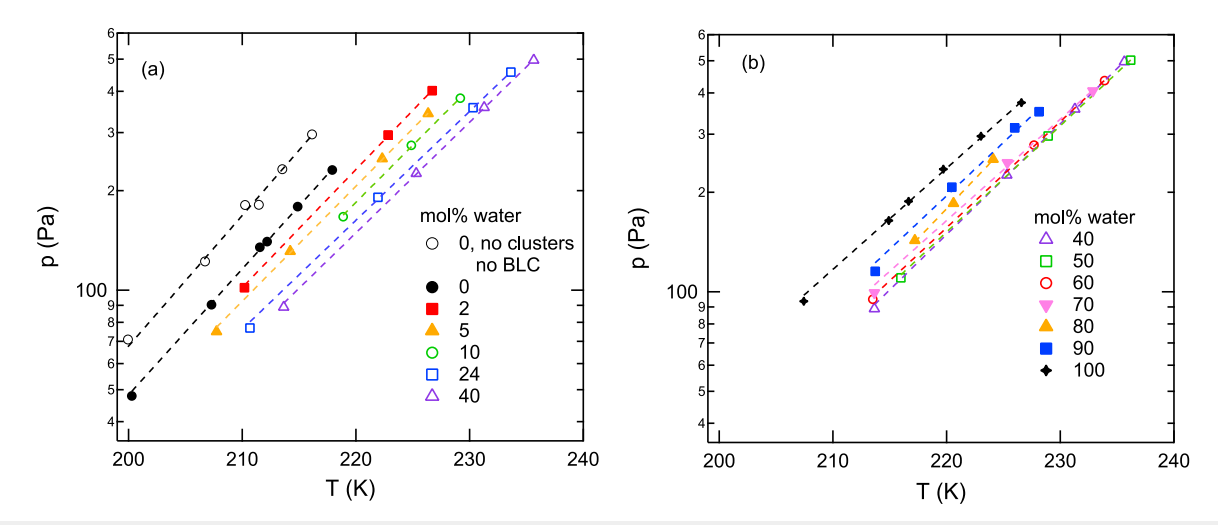
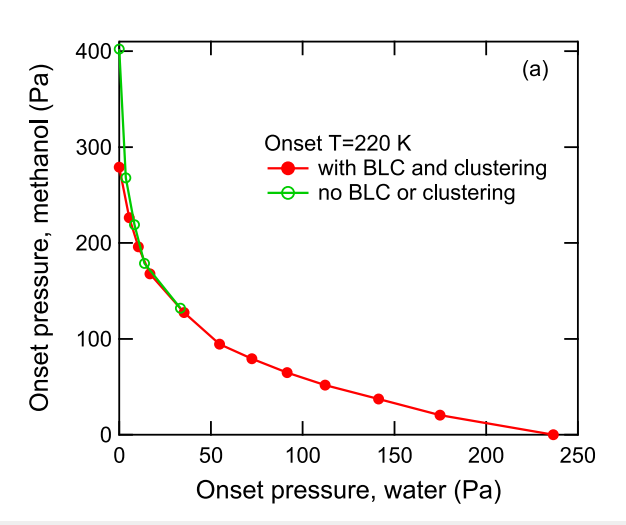


FIG. 6. Onset pressure $(p_{on,methanol} + p_{on,water})$ as a function of onset temperature for methanol—water nucleation. The onset conditions are identified by finding the maximum in methanol activity. (a) As a small amount of water is added to methanol, the onset pressure is reduced at a fixed temperature, indicating that binary nucleation occurs more easily than pure methanol nucleation. (b) In the range of 40–60 mol % water, the onset conditions barely change. As the water concentration increases further, onset curves shift back toward that for pure water.



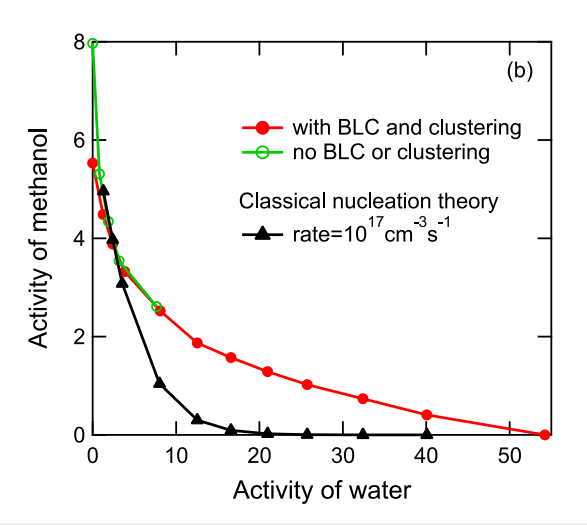


FIG. 7. (a) Onset pressure of water and methanol at an onset temperature of 220 K. The concave shape signals the enhancement of binary nucleation relative to that of the pure species. The onset conditions determined without incorporating the cluster model or correcting for boundary layer compression are also shown. Under methanol-rich conditions, these corrections are critical. (b) The experimental activities ($a_i = p_{v_i}/p_{eq,i}$) corresponding to methanol–water nucleation are compared to those predicted by the classical nucleation theory at 220 K. Agreement in the water-rich region is very poor.

values [Fig. 7(a)]. When water concentrations are above 24%, there is no significant clustering prior to the onset of droplet formation, and these corrections no longer affect the determined onset values. Figure 7(b) replots these data in terms of the activities of the two pure species ($a_i = p_{vi}/p_{eq,i}$), and it compares the current measurements to the predictions of the standard classical binary nucleation theory corresponding to a nucleation rate of 10^{17} cm⁻³ s⁻¹ at this temperature. The physical properties of methanol–water mixtures were extrapolated to 220 K as detailed in the supplementary material.

The limitations of classical nucleation theory are well documented. 43-46 In the case of binary nucleation, the standard theory⁴² assumes a uniform composition throughout the critical cluster and the surface tension is calculated as a function of the overall droplet composition. In practical terms, the standard binary theory includes surface tension derivatives in the expressions for the free energy derivatives, $\partial \Delta G/(\partial i) = 0$, that are used to determine the composition of the critical cluster, an approach that is thermodynamically inconsistent. 43,47 Unfortunately, the revised theory developed by Wilemski⁴³ that addresses this inconsistency exhibits strong unphysical behavior for methanol-water under our conditions and rates, i.e., methanol activities increase rather than decrease with increasing water activity. Other explicit cluster approaches 44,45 cannot be used here because the critical cluster sizes are expected to be too small. For the water-ethanol system under comparable experimental temperatures, Tanimura et al.38 found that over most of the composition space ($y_{\text{ethanol}} < 0.8$), critical clusters contained fewer than ~10 molecules, i.e., smaller than the minimum critical cluster size, 12, for which these theories are generally considered valid.

The agreement between theory and experiment in Fig. 7(b) is not particularly good especially in the water-rich region where the addition of very small amounts of alcohol $(10^{-4} \text{ to } 0.1)$ is predicted to reduce the required water activity far more rapidly

than what is observed experimentally. The picture is not improved by changing the form of the underlying equilibrium cluster distribution since this leads to increased nucleation rates, reducing the activities required to match the desired nucleation rates and further degrading the agreement between theory and experiment. More sophisticated approaches, for example, direct molecular dynamics simulations or Monte Carlo 10,51 approaches, should lead to better agreement with the general data trend and provide further insight into the fundamental nature of the competition between methanol clustering and binary nucleation. These calculations, however, lie well beyond the scope of the current paper.

V. SUMMARY AND CONCLUSIONS

We have investigated clustering and droplet formation from dilute methanol-water mixtures in nitrogen carrier gas flowing through a supersonic nozzle. The flow was characterized by PTM and FITR. Under methanol-rich conditions, PTMs initially indicated a gentle heat release as temperature decreases that corresponds to the formation of methanol subcritical clusters in equilibrium with methanol monomers. A stronger, more rapid heat release further downstream indicates the formation of liquid droplets. To better characterize the conditions corresponding to the onset of particle formation, we incorporated an equilibrium model for subcritical methanol cluster formation into the data analysis procedure. The enthalpy, entropy, and equilibrium constants required for this modeling are derived by combining experimental estimates for the dimer and tetramer with Helmholtz free energy differences determined via Monte Carlo simulations. The clustering model was first validated using the methanol nucleation data reported in the work of Laksmono et al.,26 where independent pressure and temperature measurements are available and the onset of droplet

formation was confirmed via small angle x-ray scattering measurements. Satisfactory agreement with the experiments was obtained using hexamers as the largest cluster size in the equilibrium cluster model.

Methanol-water binary condensation measurements were made over the entire composition range and the conditions corresponding to maximum nucleation rates were determined. These are the first reported measurements for methanol-water in an expansion experiment. Of particular interest was the effect water has on methanol clustering prior to particle formation. The pressure and temperature profiles at constant methanol vapor pressure and increasing water concentrations suggest that the addition of water does not initially perturb the heat release from subcritical cluster formation, although the current measurements cannot distinguish pure methanol cluster formation from mixed cluster formation. The temperature corresponding to the onset of droplet formation, however, increases dramatically on addition of even small amounts of water: Adding 3 mol % water increases the onset temperature by ~10 K as seen in Fig. 5. When water concentrations rise above ~24 mol %, binary droplet formation occurs at temperatures high enough that cluster formation can no longer compete. For 40-60 mol % water, the onset conditions are essentially independent of vapor composition. As water becomes the dominant species, the onset pressures increase, shifting toward the pure water line. The interpolated activities of methanol-water at 220 K reflect the strong mutual enhancement of nucleation between the two species. Standard classical binary nucleation theory does not predict the observed behavior very well—especially in the water-rich region. Other variants of classical nucleation theory do not improve this result, and explicit cluster models are difficult to apply for such small critical cluster sizes. One way forward may be to estimate the relative thermodynamic properties of the pure and mixed clusters via Monte Carlo calculations similar to those described in the supplementary material, use these to determine evaporation rate constants via detailed balance, and then calculate the nucleation rates by evolving the full set of kinetic equations. The latter approach is well beyond the scope of the current work.

SUPPLEMENTARY MATERIAL

The supplementary material summarizes the Monte Carlo method used to determine the thermodynamic cluster properties; the physical properties of methanol, water, and their mixtures; and additional model verification results.

ACKNOWLEDGMENTS

This work was completed with the financial support of the National Science Foundation under Grants Nos. CHE-1900064 (BEW) and CBET-1033387(GW).

AUTHOR DECLARATIONS

Conflict of Interest

The authors have no conflicts to disclose.

Author Contributions

Tong Sun: Conceptualization (equal); Formal analysis (equal); Investigation (lead); Software (equal); Writing – original draft (lead); Writing – review & editing (equal). Gerald Wilemski: Conceptualization (equal); Formal analysis (supporting); Investigation (lead); Methodology (supporting); Software (supporting); Supervision (supporting); Writing – original draft (supporting); Writing – review & editing (equal). Barbara N. Hale: Methodology (supporting); Software (supporting); Writing – review & editing (supporting). Barbara E. Wyslouzil: Conceptualization (equal); Formal analysis (equal); Funding acquisition (lead); Methodology (equal); Project administration (lead); Software (equal); Supervision (equal); Writing – original draft (equal); Writing – review & editing (equal).

DATA AVAILABILITY

The data that support the findings of this study are available from the corresponding author upon reasonable request.

REFERENCES

- ¹R. Strey, T. Schmeling, and P. E. Wagner, J. Chem. Phys. **85**, 6192 (1986).
- ²R. Strey, P. E. Wagner, and T. Schmeling, J. Chem. Phys. **84**, 2325 (1986).
- ³G. Palinkas, E. Hawlicka, and K. Heinzinger, J. Phys. Chem. 91, 4334 (1987).
- ⁴U. Buck and F. Huisken, Chem. Rev. 100, 3863 (2000).
- ⁵R. Ludwig, ChemPhysChem **6**, 1369 (2005).
- ⁶K. Ohno, T. Shimoaka, N. Akai, and Y. Katsumoto, J. Phys. Chem. A 112, 7342 (2008).
- ⁷M. M. Pires and V. F. DeTuri, J. Chem. Theory Comput. 3, 1073 (2007).
- ⁸M. A. Suhm, Adv. Chem. Phys. 142, 1 (2009).
- ⁹S. Kazachenko, S. Bulusu, and A. J. Thakkar, J. Chem. Phys. 138, 224303 (2013).
- ¹⁰ J. F. Counsell and D. A. Lee, J. Chem. Thermodyn. 5, 583 (1973).
- ¹¹F. Huisken, M. Kaloudis, M. Koch, and O. Werhahn, J. Chem. Phys. **105**, 8965 (1996).
- ¹²I. Y. Doroshenko, Low Temp. Phys. 37, 604 (2011).
- ¹³ H.-L. Han, C. Camacho, H. A. Witek, and Y.-P. Lee, J. Chem. Phys. **134**, 144309 (2011).
- ¹⁴W. Weltner, Jr. and K. S. Pitzer, J. Am. Chem. Soc. 73, 2606 (1951).
- ¹⁵T. A. Renner, G. H. Kucera, and M. Blander, J. Chem. Phys. **66**, 177 (1977).
- ¹⁶E. E. Tucker, S. B. Farnham, and S. D. Christian, J. Phys. Chem. 73, 3820 (1969).
- ¹⁷R. A. Provencal, J. B. Paul, K. Roth, C. Chapo, R. N. Casaes, R. J. Saykally, G. S. Tschumper, and H. F. Schaefer III, J. Chem. Phys. 110, 4258 (1999).
- ¹⁸T. Häber, U. Schmitt, and M. A. Suhm, Phys. Chem. Chem. Phys. 1, 5573 (1999).
- ¹⁹R. W. Larsen, P. Zielke, and M. A. Suhm, J. Chem. Phys. **126**, 194307 (2007).
- ²⁰F. Huisken, A. Kulcke, C. Laush, and J. M. Lisy, J. Chem. Phys. **95**, 3924 (1991).
- ²¹T. Kobayashi, R. Shishido, K. Mizuse, A. Fujii, and J.-L. Kuo, Phys. Chem. Chem. Phys. 15, 9523 (2013).
- ²²B. D. Kay and A. W. Castleman, Jr., J. Phys. Chem. **89**, 4867 (1985).
- ²³ M. Mandado, A. M. Graña, and R. A. Mosquera, Chem. Phys. Lett. 381, 22 (2003)
- ²⁴S. L. Boyd and R. J. Boyd, J. Chem. Theory Comput. 3, 54 (2007).
- ²⁵M. Umer and K. Leonhard, J. Phys. Chem. A **117**, 1569 (2013).
- ²⁶ H. Laksmono, S. Tanimura, H. C. Allen, G. Wilemski, M. S. Zahniser, J. H. Shorter, D. D. Nelson, J. B. McManus, and B. E. Wyslouzil, Phys. Chem. Chem. Phys. 13, 5855 (2011).
- ²⁷B. N. Hale and D. J. DiMattio, J. Phys. Chem. B **108**, 19780 (2004).

- ²⁸B. N. Hale and M. Thomason, Phys. Rev. Lett. **105**, 046101 (2010).
- ²⁹B. Hale, G. Wilemski, and A. Viets, AIP Conf. Proc. **1527**, 27–30 (2013).
- ³⁰Y. Park and B. E. Wyslouzil, Phys. Chem. Chem. Phys. **21**, 8295 (2019).
- ³¹ S. Tanimura, Y. Zvinevich, B. E. Wyslouzil, M. Zahniser, J. Shorter, D. Nelson, and B. McManus, J. Chem. Phys. 122, 194304 (2005).
- ³²C. Flageollet, M. D. Cao, and P. Mirabel, J. Chem. Phys. **72**, 544 (1980).
- ³³D. Ghosh, A. Manka, R. Strey, S. Seifert, R. E. Winans, and B. E. Wyslouzil, J. Chem. Phys. **129**, 124302 (2008).
- ³⁴ A. Manka, H. Pathak, S. Tanimura, J. Wölk, R. Strey, and B. E. Wyslouzil, Phys. Chem. Chem. Phys. 14, 4505 (2012).
- ³⁵ A. J. Amaya and B. E. Wyslouzil, J. Chem. Phys. **148**, 084501 (2018).
- ³⁶ H. Laksmono, S. Tanimura, and B. E. Wyslouzil, J. Chem. Phys. **135**, 074305 (2011).
- 37 A. J. Amaya, "Freezing supercooled water nanodroplets near \sim 225 K through homogeneous and heterogeneous ice nucleation," Ph.D. dissertation (The Ohio State University, 2018).
- ³⁸S. Tanimura, H. Pathak, and B. E. Wyslouzil, J. Chem. Phys. **139**, 174311 (2013).

- ³⁹C. H. Heath, K. Streletzky, B. E. Wyslouzil, J. Wölk, and R. Strey, J. Chem. Phys. 117, 6176 (2002).
- ⁴⁰R. Strey, Y. Viisanen, and P. E. Wagner, J. Chem. Phys. **103**, 4333 (1995).
- ⁴¹ B. E. Wyslouzil, C. H. Heath, J. L. Cheung, and G. Wilemski, J. Chem. Phys. **113**, 7317 (2000).
- ⁴²H. Reiss, J. Chem. Phys. 18, 840 (1950).
- ⁴³G. Wilemski, J. Phys. Chem. **91**, 2492 (1987).
- ⁴⁴C. Flageollet-Daniel, J. P. Garnier, and P. Mirabel, J. Chem. Phys. **78**, 2600 (1983)
- ⁴⁵ A. Laaksonen and M. Kulmala, J. Chem. Phys. **95**, 6745 (1991).
- $^{\mathbf{46}}\mathrm{X.}$ C. Zeng and D. W. Oxtoby, J. Chem. Phys. **95**, 5940 (1991).
- ⁴⁷G. Wilemski, J. Chem. Phys. **80**, 1370 (1984).
- ⁴⁸B. E. Wyslouzil and G. Wilemski, J. Chem. Phys. **103**, 1137 (1995).
- ⁴⁹ M. Tarek, S. Bandyopadhyay, and M. L. Klein, J. Mol. Liq. **78**, 1 (1998).
- ⁵⁰B. Chen, J. I. Siepmann, and M. L. Klein, J. Am. Chem. Soc. **125**, 3113 (2003).
- ⁵¹S. M. Kathmann, G. K. Schenter, B. C. Garrett, B. Chen, and J. I. Siepmann, J. Phys. Chem. C 113, 10354 (2009).